

DESIGN AND TIME-DOMAIN ANALYSIS OF A HIGH-VOLTAGE IMPULSED TEST-BED FOR NEAR-FIELD THERMOACOUSTIC TOMOGRAPHY

Amir Hajiaboli^{*}, Stephan Kellnberger, Vasilis Ntziachristos, and Daniel Razansky[†]

Technical University of Munich and Helmholtz Center Munich, Germany

Abstract—We present numerical time-domain modeling and validation framework for impulse-driven near-field thermoacoustics imaging. It has been recently demonstrated that this new imaging approach comprises a viable alternative for high performance and low-cost imaging using the thermoacoustic phenomenon. Placement of the imaged object in a close vicinity (near field) of an antenna elements along with generation of ultrashort (nanosecond) duration high-voltage excitation impulses further provide high imaging resolution and ensure that sufficient level of electromagnetic energy reaches the object under investigation. In order to analyze the measured results and also provide a design and optimization framework, this work presents a full-wave computational electromagnetic framework which couples the near-field electromagnetic field to the acoustic signal generation. The numerical method comprises a finite integral time domain method (FITD) based on the industry standard CST 2010 software package. The results can be further utilized for normalization and quantification of the generated images.

1. INTRODUCTION

Thermoacoustics imaging is a hybrid modality which capitalizes on the contrast of microwave imaging combined with high resolution associated with ultrasound imaging. Thermo-acoustic signal is generated when short pulses of electromagnetic energy are absorbed by the imaged tissue, which creates instantaneous expansion. This

Received 6 January 2013, Accepted 19 February 2013, Scheduled 23 April 2013

^{*} Corresponding author: Amir Hajiaboli (amir.hajiaboli@ieee.org).

[†] Daniel Razansky (dr@tum.de) was the supervisor of the work.

yields a propagating pressure wave that can be detected by sensitive ultrasound detectors.

While these were initially microwave-induced thermo-acoustic systems, which conceptually proved the success of combining electromagnetic waves with sound for imaging purposes [1–3], currently, it is the laser-induced counterpart (optoacoustics) which is mostly under investigation [4–6]. Yet, laser induced optoacoustic systems have an inherent limitation on the depth of penetration due to the high attenuation of light energy inside biological tissues. In the recent years, laser-induced thermoacoustic systems have evolved to provide deeper penetration and capture images from within several centimeters [7, 8]. Nevertheless, this depth is still not adequate for many clinical applications.

Thermoacoustic systems, operating in the radiofrequency and microwave bands, have the advantage of significantly higher penetration depth into the tissue. Yet, the major difficulty has been coupling sufficient electromagnetic power into the biological sample to generate a detectable acoustic pressure. The current state-of-the-art microwave-induced thermoacoustic systems utilize coupling of radiative energy into the imaged volume and therefore employ relatively expensive ultra-high peak power modulated microwave sources [1, 9–11] to drive the antenna elements. Furthermore, the peak power of the available microwave modulators is limited and, consequently, to generate sufficient per-pulse energy, the pulse duration is usually extended into the microsecond range [1], setting a hard compromise between spatial resolution and signal-to-noise ratio of the system and limiting the spatial resolution achieved [12].

To shrink the pulse duration, instead of modulated pulses, the idea of utilizing ultra wide-band (UWB) high voltage impulses to couple sufficient electromagnetic energy into the biological tissue has been proposed [13, 14]. In contrary to the traditional thermoacoustic imaging methods this new modality works based on coupling of a non-radiative energy stored in the vicinity of the antenna element into the imaged object.

In this paper, we present a numerical framework based on industry-standard computational electromagnetic software (CST 2010) for assessment and optimization of near field absorptive coupling into the biological sample. An experimental procedure for assessment of the suggested simulation framework is further introduced. Furthermore, a reproducible approach for developing a radio-frequency test-bed is presented and validated with simulation results.

2. THEORY AND METHODS

2.1. Thermoacoustic Signal Generation

Mathematically, thermoacoustic signal generation and propagation are described via:

$$\nabla^2 p(r, t) - \frac{1}{v^2} \frac{\partial^2 p}{\partial t^2}(r, t) = \frac{\beta}{C_p} \frac{\partial H(r, t)}{\partial t} \quad (1)$$

Although various sources utilize different nomenclature [15–18], here β denotes the thermal expansion coefficient of the medium, C_p is the specific heat, v is the speed of sound, and H stands for the spatio-temporal dependence of the electromagnetic power absorption density (heating function). Assuming the pulse is short enough so that heat exchange with the surrounding biological tissue can be ignored, the heating function can be separated into a time dependent and space related functions, i.e.,

$$H(r, t) = A(r)\delta(t) \quad (2)$$

where the Dirac-delta function approximates the temporal profile of the deposited energy and $A(r)$ describes its spatial distribution. Under those assumptions, Eq. (1) can be rewritten as

$$\nabla^2 p(r, t) - \frac{1}{v^2} \frac{\partial^2 p}{\partial t^2}(r, t) = -p_0 \delta'(t) \quad (3)$$

where $p_0 = \beta/C_p v^2 A(r)$. In cases of excitation of electrically conducting media in the radio-frequency and microwave spectra, the total electromagnetic energy deposited into the biological sample during the pulse can be further written as

$$A(r) \approx \sigma(r) \int_{\tau} E^2(r, t) dt \quad (4)$$

Here, τ is the total duration of the pulse while $\sigma(r)$ and $E(r)$ are conductivity and electric field at location r , respectively. In Eq. (4), frequency changes of electric losses have been neglected for simplicity.

From (3) and (4) one can conclude that thermoacoustic response can be increased by prolonging τ or increasing the excitation field E . However, increasing the pulse duration readily deteriorates the spatial resolution [12]. Instead, our NRT system utilizes a high voltage impulse generator, a solution which sustains good resolution and also provides sufficient energy for the generation of pressure waves [19].

2.2. Experimental Setup of the Radio-frequency Test-bed and Its Numerical Model

Figure 1(a) shows the experimental thermoacoustic setup and highlights the main components of the system. Figure 1(b) shows the schematic of the electrical connection between the main components of the system. The high voltage switch used is a spark gap with a fast transient switching time. The charging capacitor (550 pF) charges through the high voltage DC source (30 kV), a limiting resistor (4 M Ω) and a terminating resistor (470 Ω). By triggering the switch, the energy stored in the capacitor discharges into the antenna element, which couples the stored energy into the biological sample placed in its vicinity. This subsequently generates a pressure wave, which is detected by an ultrasonic transducer. The entire setup is enclosed with aluminum plates to avoid interferences with the nearby electronic circuits and measurement equipment. Due to the high electric field, the connecting wires are also covered with shielding tubes. More details of the experimental setup can be found in References [13, 14].

Figure 2 shows the schematic of the numerical model of the experimental setup used in our study. The main parameters to be considered are: the proper choice of matching medium, antenna element and overall shape of the container.

To date, two types of matching media have been used for thermoacoustic imaging, i.e., distilled water ($\epsilon_r = 81$) and mineral oil ($\epsilon_r = 2.03$) [15, 20]. The choice of the matching medium is yet another subject of our investigation. A helical antenna element has been selected and its optimization parameter is the number of turns of the helix in a fixed height and radius [14].

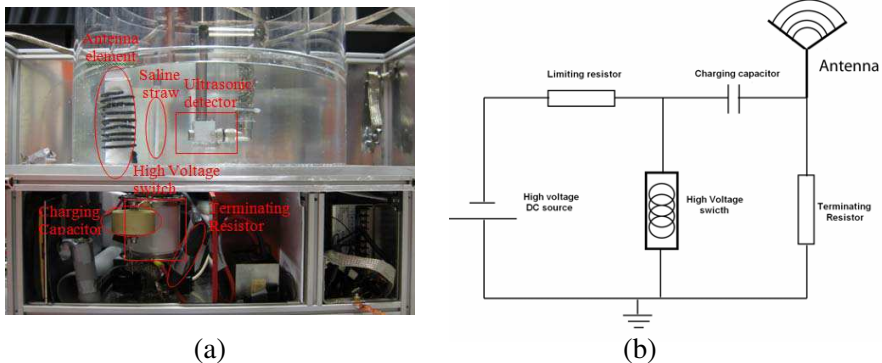


Figure 1. (a) Experimental setup, (b) schematics of the main electrical components of the high voltage pulse generator.

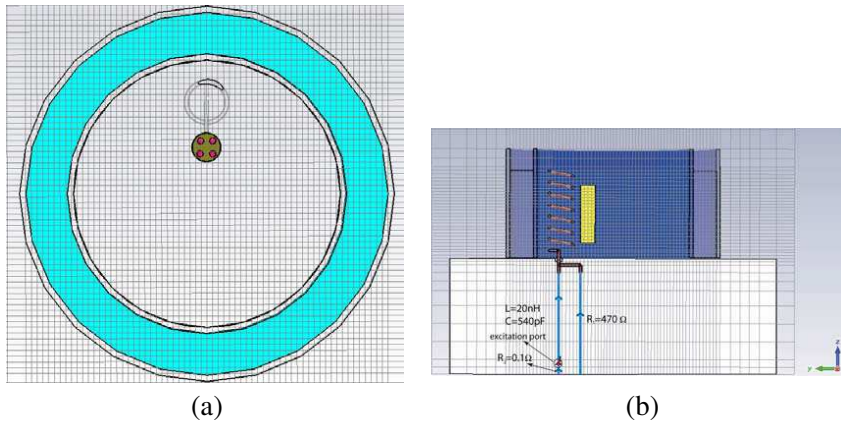


Figure 2. (a) The FDTD model of the test-bed along with (b) the lumped circuit model of the pulse generator.

Furthermore, to prevent the water container from acting as a resonator, which eventually reduces the bandwidth of the antenna and increases the pulse duration, a double layer design has been used instead, as shown in Figure 2. The inner volume, enclosing the sample and antenna, is filled with distilled water while the outer layer contains salty water, which absorbs the outgoing waves and inhibits reflection on the air-water boundary. We will show how this new configuration can help with better confinement of the initial pressure induced in the biological sample.

The antenna input impedance would be affected by all the parameters in the test-bed, namely, the shape of water container, the matching medium and more importantly by its own shape. Although in this paper we have focused our simulations on an end-to-end performance, which shows the effect of each of these parameters on the final image obtained, for the actual imaging performance it might still be helpful to understand the effects of antenna impedance on the impulse shape at its input. We have therefore also simulated impulse generator using an equivalent electric circuit shown in Figure 1(b) using PSpice software.

2.3. Numerical Simulation: Finite-integration Time-domain

To assist with design and optimization of the NRT imaging approach, we have employed time domain (TD) numerical technique to model the transient field distribution. The technique adopted is based on finite-integral time domain (FITD) implemented by the Computer

Simulation Technology Inc. [21] in its software package CST Microwave Studio 2010.

In principle, FITD is very similar to the Finite-Different Time-Domain (FDTD) technique [22] except the fact that FITD works with the integral form of Maxwell's equations while FDTD employs their differential equivalent. Utilizing the integral form helps with modeling curved structures and has already been implemented in FDTD as a special case of subcell modeling [23]. Both techniques have the advantage of flexibility in modeling highly heterogeneous environments, such as those involving biological tissues. In addition, as being an intrinsically time-domain technique, it is highly desirable for the particular case of simulating the broadband pulse excitation utilized in our study.

The lumped elements of the generator are also incorporated into the simulation as shown in Figure 2(b). For this, the basic current and voltage relationship has been further discretized and incorporated into the FITD updating equations [23].

Since the test-bed was enclosed into a shielding conductor box to avoid interferences with the nearby measurement instruments, a PEC boundary condition was employed to truncate the simulation space in all directions except the upper boundary which is terminated with a perfectly matched layer PML [23].

To sustain stability of the simulation, the time step has been chosen based on the Courant-Friedrichs-Levy criterion [23] via

$$\Delta t \leq \frac{\sqrt{\varepsilon\mu}}{\sqrt{\left(\frac{1}{\Delta x}\right)^2 + \left(\frac{1}{\Delta y}\right)^2 + \left(\frac{1}{\Delta z}\right)^2}} \quad (5)$$

where, Δx , Δy and Δz are the minimum of dimensions of mesh cells in x , y and z directions, respectively.

The computer setup utilized in the simulation is a Pentium IV

Table 1. Information on simulation space setup.

Number of cells	$N_x = 86$, $N_y = 79$, $N_z = 84$ (550,290 cells in total)
Minimum dimensions	$dx = 2$ mm, $dy = 2$ mm, $dz = 1$ mm
Time step	4.803466 ps
Total simulation time	~ 30 min on a Pentium IV Quad-Core accelerated with Tesla 1060 graphic accelerator card.

Quad-Core with 8 Giga-Byte RAM and, in order to further accelerate simulations, a Tesla 1060 graphic accelerator card has been utilized. The latter achieved, on average, 5 fold reduction in the calculation times. Table 1 summarizes the details of simulation setup utilized in this study.

A short time (10 ns) Gaussian band pulse has been selected in order to generate ultrawideband excitation.

3. RESULTS

3.1. Experimental Validation of the Numerical Model

As shown in the PSpice simulation results in Figure 3, the impulse shape is significantly affected by the input impedance of the antenna, which is modeled here by a simple resistive load. Clearly, higher impedance leads to longer capacitor discharge times, prolonging the overall impulse duration. On the other hand, low impedance might lead to under-damping, significant reduction of peak impulse voltage and oscillations, as in the case of $Z_{\text{antenna}} = 5 \Omega$. Thus, for the current pulse generator configuration, optimal antenna impedance would be around 10Ω , providing impulse with FWHM of about 10 ns and peak voltage of 20 kV. This pulse is therefore selected as the desirable pulse shape for excitation in the time-domain electromagnetic analysis.

Figure 4 shows the Fourier transform of the signal recorded by the electric field probe and its comparison with FITD simulation for a seven turn helical antenna with 110 mm height and radius of 16 mm. The two signals match well with each other while the discrepancies at the higher frequency range can be attributed to some simplified

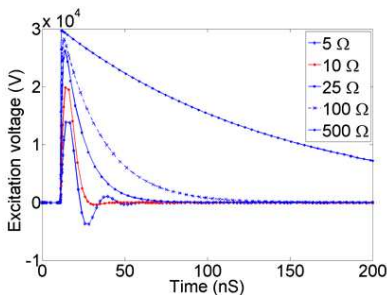


Figure 3. The effect of the antenna input impedance on the generated impulse shape: PSpice simulation.

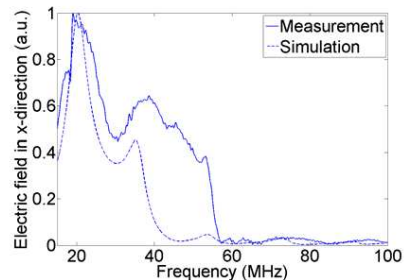


Figure 4. Electric field recorded outside the water container: measurement versus simulation.

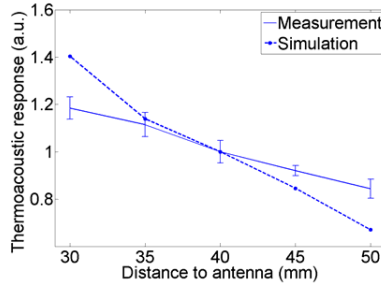


Figure 5. Thermoacoustic signal from a saline straw versus distance to the antenna. The measured signal has been repeated for 3 times and the vertical lines indicate the error margin.

assumptions in modeling the high voltage components utilized in the setup.

For further experimental validation of the numerical framework, the acoustic pressure generated has been measured using the experimental setup depicted in Figure 1(a). The ultrasonic transducer is a cylindrically focused transducer (central frequency 3.5 MHz, focal distance 38.1 mm, bandwidth 76.3%; Model V382, Olympus-NDT, Waltham, MA, USA). A saline solution inside a narrow straw has been placed in the focus of the transducer and both the transducer and the saline solution have been moved along a line in front of the antenna.

To increase the signal to noise ratio, the measured signals have been averaged for 100 consecutive pulses. Furthermore, the measurement scenario has been repeated for 3 times to reduce experimental uncertainties. The vertical lines in Figure 5 indicate the maximum and minimum of readings, which have been obtained at each distance from the antenna.

A similar scenario has been simulated ($\varepsilon_{r\text{-straw}} = 81$, $\sigma_{\text{straw}} = 1 \text{ S/m}$) in the numerical framework and the total electric losses, which are proportional to the induced pressure, have been integrated over the saline straw. As depicted in Figure 5, the normalized results in simulation and measurement have a fairly good agreement.

3.2. Time-domain Impulse Propagation inside the Biological Sample

Next, a time domain analysis of a phantom consisting of three concentric cylinders was performed in order to simulate UWB impulse propagation through the setup and biological sample. For this, a numerical phantom was constructed having typical small animal tissue

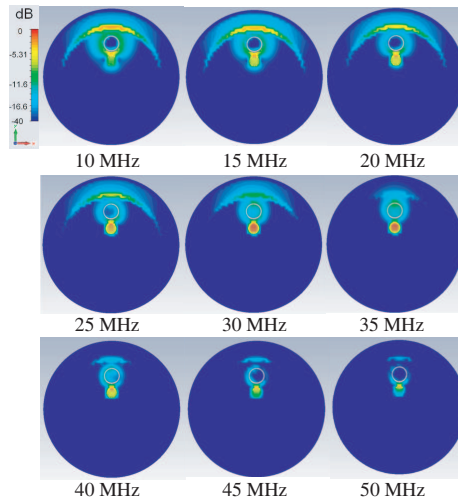


Figure 6. Distribution of the electric loss absorption at different frequencies.

parameters, i.e., the outer layer mimicking skin layer ($\epsilon_r = 120$ F/m, $\sigma = 0.5$ S/m) of 0.5 mm thickness; the fat layer ($\epsilon_r = 40$ F/m, $\sigma = 0.025$ S/m) of 1 mm and a 10 mm diameter cylinder mimicking muscle tissue in the center ($\epsilon_r = 170$ F/m, $\sigma = 0.5$ S/m). The dielectric properties of each layer were chosen in accordance with the available data on the dielectric properties of biological tissue at around 25 MHz [24].

Figure 6 depicts the frequency domain analysis with power absorption density (electric losses) inside the test-bed and biological sample calculated at different frequencies. As can be observed, the energy is predominantly absorbed in the biological sample and, to some extent, also in the deionized water close to the antenna. Furthermore, the absorption is dominant in the frequency range between 25 MHz to 35 MHz, which agrees well with probe measurement in Figure 4. The supplementary movie shows the full course of impulse propagation inside the test-bed and the biological sample for the duration of 100 ns.

3.3. Parametric Analysis of the Setup

Using the numerical framework, theoretically developed in II, one can analyze the effect of different components of the test-bed and antenna structure on the initial pressure wave induced inside the biological sample. Here the numerical phantom consists of four muscle tissue insertions inside fat and a thin layer of skin (0.5 mm). To minimize

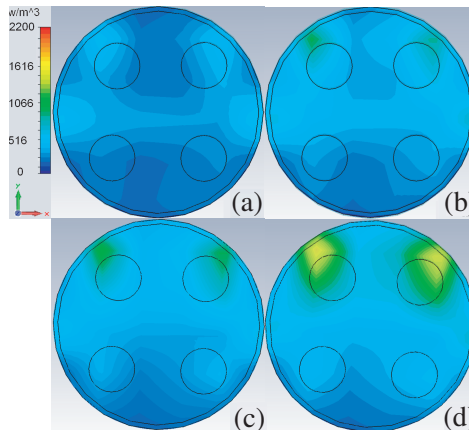
the error in fitting the dispersion properties of biological tissues, a first order curve fitting for fat and a second order curve fitting for muscle and skin has been adopted based on the algorithm developed in CST microwave studio software.

Even though in electromagnetic simulation we have utilized dispersion of the biological sample for both permittivity and electric losses, the frequency changes of electric loss are very negligible over the broad range of simulated frequencies (10–100 MHz) [24]. This means, one can utilize the Parseval's theorem to calculate the initial pressure wave by adding the frequency components of electric losses based on Eq. (4).

Using this framework, the effects of different parameters of thermoacoustic test-bed can be readily and efficiently examined, which are otherwise expensive or impossible to investigate experimentally. The basic criteria for the analysis are the maximum level and the confinement of the initial pressure induced, the main factors affecting the spatial resolution of the final images. In all the analysis provided here, the pressure wave induced in a cross section of the numerical phantom located in front of the ultrasonic detector has been calculated.

3.3.1. Different Number of Turns for the Antenna Element

Figure 7 shows the initial pressure induced for different helical structures with different number of turns but similar radius (16 mm) and height (110 mm). As can be observed, the initial pressure increases by increasing the number of turns. Furthermore, increasing the number of turns shifts the maxima of the generated pressure wave toward the area of muscle, which is a desirable effect and helps with creating a better tissue contrast.



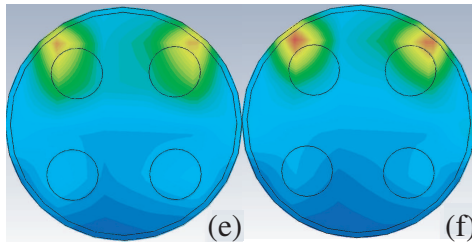


Figure 7. Initial pressure induced for different number of turns of antenna: (a) 2 turns, (b) 4 turns, (c) 6 turns, (d) 8 turns, (e) 10 turns and (f) 12 turns.

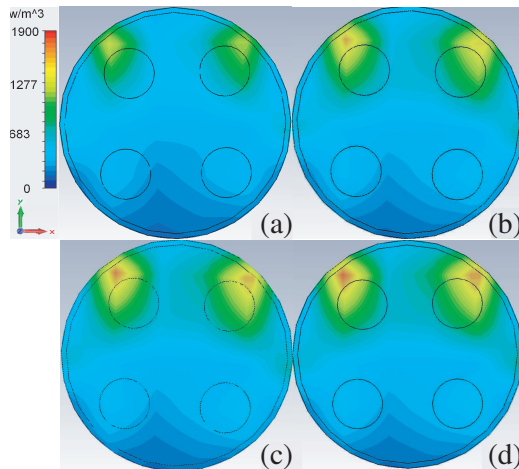


Figure 8. Initial pressure induced for different terminating resistor: (a) $50\ \Omega$, (b) $250\ \Omega$, (c) $500\ \Omega$ and (d) $10\ \text{k}\Omega$.

3.3.2. Variations of the Terminating Resistor

Figure 8 shows the initial pressure wave for different values of the terminating resistor shown in Figure 1(b). As one can observe, by increasing the terminating resistance the initial pressure increases. The side effect of increasing the terminating resistor is the prolongation of the time constant required for charging the capacitor, which reduces the capabilities of the system to be utilized as a real-time imaging system. Furthermore, one can observe that increasing the terminating resistor does not affect the confinement of the initial pressure induced.

3.3.3. Variations of the Charging Capacitor

Figure 9 shows the effect of increasing the charging capacitor. It can be seen that by increasing the charging capacitor the initial pressure inside the sample reduces. However, reducing the charging capacitor linearly reduces the total available power. Furthermore, one can observe that different values of charging capacitance do not affect the confinement of the initial pressure induced.

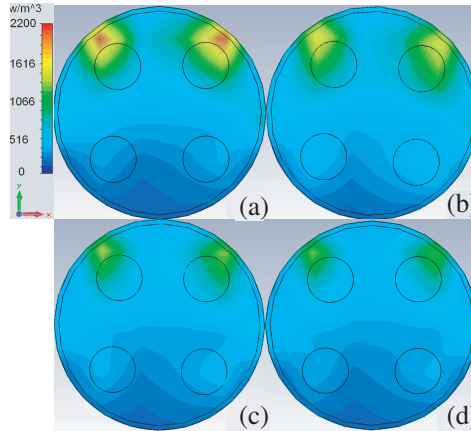


Figure 9. Initial pressure induced for different values of charging capacitors: (a) 100 nF, (b) 550 nF, (c) 1000 nF and (d) 2000 nF.

3.3.4. Double Layer Water Tank versus Single Layer Water Tank

Figure 10 presents the effect of including an absorbing layer of water ($\sigma = 1 \text{ S/m}$) on the outer side of the water tank, creating a double layer configuration. Although adding this layer reduces the initial pressure induced, it still helps with better confinement of the pressure wave in the areas close to the muscle tissues. This can be due to inhibition of electromagnetic wave reflections on the water-air boundary.

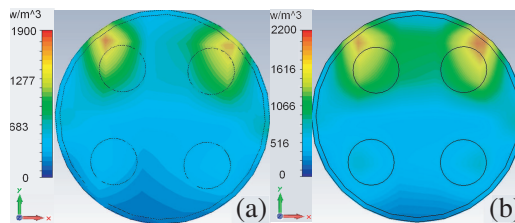


Figure 10. Initial pressure induced for two different water container configurations: (a) double layer water tank, (b) single layer water tank.

3.3.5. Mineral Oil versus Distilled Water as Coupling Medium

Figure 11 shows the effect of using mineral oil versus distilled water as coupling medium. As can be observed, presence of mineral oil substantially deteriorates both strength and temporal confinement of the initial pressure induced inside the biological sample.

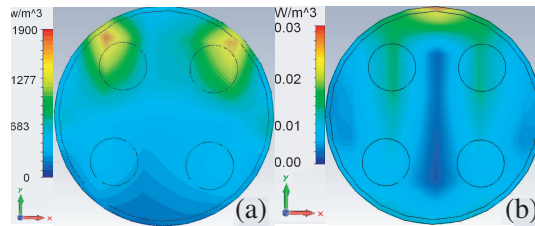


Figure 11. Initial pressure induced for two different coupling media: (a) distilled water, (b) mineral oil.

4. CONCLUSION

In this paper, we have developed a computational framework for analysis and optimization of the recently introduced impulse-driven near-field thermoacoustic tomography (NRT). The approach is based on finite-integration time-domain (FITD) technique, which has been adopted for studying interactions of biological tissues located in the near-field of an ultra-wideband electromagnetic source. In order to provide an accurate assessment of the end-to-end system performance, the coupled simulation included both lumped elements of the impulse generator and full wave computational electromagnetic analysis of the test-bed. The theory of coupling the dissipated electromagnetic energy into the initial pressure induced inside the biological sample has been presented and a tissue-mimicking numerical phantom has been developed. The presented simulation framework was further evaluated based on the experimental NRT test-bed, showing good correspondence between simulation and experiment.

Finally, a parametric analysis has been employed in order to provide guidelines for designing different NRT system components. The optimization is based on the strength and confinement of the initial pressure induced in the biological sample. The developed framework allows calculating heterogeneous distribution of the excitation field, thus can be further utilized to normalize and better quantify images obtained with NRT systems.

REFERENCES

1. Kruger, R. A., K. D. Miller, H. E. Reynolds, W. L. Kiser, Jr., D. R. Reinecke, and G. A. Kruger, "Breast cancer in vivo: Contrast enhancement with thermoacoustic CT at 434 MHz-feasibility study," *Radiology*, Vol. 216, 279–283, Jul. 2000.
2. Robert, P., A. Kruger, M. Kathy, D. Miller, M. Handel, E. Reynolds, J. William, L. Kiser, M. Daniel, R. Reinecke, and G. A. Kruger, "Breast cancer in vivo: Contrast enhancement with thermoacoustic CT at 434 MHz-feasibility study," *Radiology*, Vol. 216, 279–283, 2000.
3. Kruger, R. A. and W. L. Kiser, "Thermoacoustic CT of the breast: Pilot study observations," *Proc. SPIE*, Vol. 4256, 1–5, 2001.
4. Wang, L. V., "Prospects of photoacoustic tomography," *Medical Physics*, Vol. 35, 5758–5767, Dec. 2008.
5. Patch, S. K. and O. Scherzer, "Photo- and thermo-acoustic imaging," *Inverse Problems*, Vol. 23, S01–S10, 2007.
6. Wang, L. V., "Tutorial on photoacoustic microscopy and computed tomography," *IEEE Journal of Selected Topics in Quantum Electronics*, Vol. 14, 171–179, Jan.–Feb. 2008.
7. Razansky, D., M. Distel, C. Vinegoni, R. Ma, N. Perrimon, R. W. Koster, and V. Ntziachristos, "Multispectral opto-acoustic tomography of deep-seated fluorescent proteins in vivo," *Nature Photonics*, Vol. 3, 412–417, Jul. 2009.
8. Ntziachristos, V. and D. Razansky, "Molecular imaging by means of multispectral optoacoustic tomography (MSOT)," *Chem. Rev.*, Vol. 110, 2783–2794, May 2012.
9. Jin, X., C. H. Li, and L. V. Wang, "Effects of acoustic heterogeneities on transcranial brain imaging with microwave-induced thermoacoustic tomography," *Medical Physics*, Vol. 35, 3205–3214, Jul. 2008.
10. Feng, D., Y. Xu, G. Ku, and L. V. Wang, "Microwave-induced thermoacoustic tomography: Reconstruction by synthetic aperture," *Medical Physics*, Vol. 28, 2001.
11. Wang, L. V., X. Zhao, H. Sun, and G. Ku, "Microwave-induced acoustic imaging of biological tissues," *Review of Scientific Instruments*, Vol. 70, 3744–3748, 1999.
12. Kruger, R. A., W. L. Kiser, K. D. Miller, and H. E. Reynolds, "Thermoacoustic CT: Imaging principles," *Proc. SPIE on Biomedical Optoacoustics*, 150–159, 2000.
13. Razansky, D., S. Kellnberger, and V. Ntziachristos, "Near-field radiofrequency thermoacoustic tomography with impulse excitation," *Medical Physics*, Vol. 37, 4602–4607, Sep. 2010.

14. Kellnberger, S., A. Hajiaboli, D. Razansky, and V. Ntziachristos, "Near-field thermoacoustic tomography of small animals," *Physics in Medicine and Biology*, Vol. 56, 3433, 2011.
15. Fallon, D., L. Yan, G. W. Hanson, and S. K. Patch, "RF testbed for thermoacoustic tomography," *Rev. Sci. Instrum.*, Vol. 80, 064301, Jun. 2009.
16. Mashal, A., J. H. Booske, and S. C. Hagness, "Toward contrast-enhanced microwave-induced thermoacoustic imaging of breast cancer: An experimental study of the effects of microbubbles on simple thermoacoustic targets," *Phys. Med. Biol.*, Vol. 54, 641–650, Feb. 7, 2009.
17. Zeng, X. and G. Wang, "Numerical study of microwave-induced thermoacoustic effect for early breast cancer detection," *IEEE Antennas and Propagation Society International Symposium*, 2005.
18. Yan, J., C. Tao, and S. Wu, "Energy transform and initial acoustic pressure distribution in microwave-induced thermoacoustic tomography," *Proceedings of the 2005 IEEE Engineering in Medicine and Biology 27th Annual Conference*, Shanghai, China, 2005.
19. Jung, M., T. H. G. G. Weise, U. Braunsberger, and F. Sabath, "High power compact UWB systems," *International Conference on Pulsed Power Applications*, Mar. 29–30, 2001.
20. Xu, Y. and L. V. Wang, "Rhesus monkey brain imaging through intact skull with thermoacoustic tomography," *IEEE Transactions on Ultrasonics Ferroelectrics and Frequency Control*, Vol. 53, 542–548, Mar. 2006.
21. Munteanu, I. and T. Weiland, "RF & microwave simulation with the finite integration technique — From component to system design," *Scientific Computing in Electrical Engineering*, 247–260, 2007.
22. Marklein, R., "The finite integration technique as a general tool to compute acoustic, electromagnetic, elastodynamic, and coupled wave fields," *Review of Radio Science*, 201–244, IEEE Press, Piscataway, 2002.
23. Taflov, A. and S. C. Hagness, *Computational Electrodynamics: The Finite-Difference Time-Domain Method*, 3rd Edition, Artech House, 2007.
24. Gabriel, S., R. W. Lau, and C. Gabriel, "The dielectric properties of biological tissues. 3. Parametric models for the dielectric spectrum of tissues," *Physics in Medicine and Biology*, Vol. 41, 2271–2293, Nov. 1996.